Diffusion-driven self-assembly of emerin nanodomains at the nuclear envelope

Carlos D. Alas [1,2] Liying Wu,[3] Fabien Pinaud [1,3,4,*] and Christoph A. Haselwandter [1,2,†]

[1]*Department of Physics and Astronomy, University of Southern California, Los Angeles, California 90089, USA*
[2]*Department of Quantitative and Computational Biology, University of Southern California, Los Angeles, California 90089, USA*
[3]*Department of Biological Sciences, University of Southern California, Los Angeles, California 90089, USA*
[4]*Department of Chemistry, University of Southern California, Los Angeles, California 90089, USA*

Emerin, a nuclear membrane protein with important biological roles in mechanotransduction and nuclear shape adaptation, self-assembles into nanometer-size domains at the inner nuclear membrane. The size and emerin occupancy of these nanodomains change with applied mechanical stress as well as under emerin mutations associated with Emery-Dreifuss muscular dystrophy (EDMD). Through a combination of theory and experiment, we show here that a simple reaction-diffusion model explains the self-assembly of emerin nanodomains. Our model yields quantitative agreement with experimental observations on the size and occupancy of emerin nanodomains for wild-type emerin and EDMD-associated mutations of emerin, with and without applied forces, and allows successful prediction of emerin diffusion coefficients from observations of the overall properties of emerin nanodomains. Our results provide a physical understanding of EDMD-associated defects in emerin organization in terms of changes in key reaction and diffusion properties of emerin and its nuclear binding partners.

Emerin is a largely disordered protein predominantly located at the nuclear envelope (NE) in mammalian cells and in cells of various other eukaryotic organisms [1,2]. It is a major contributor to the maintenance of nuclear mechanics, as it participates in the transduction of mechanical signals across the nucleus double membrane [3,4]. Emerin mostly resides in the inner nuclear membrane (INM), where it interacts with multiple nuclear binding partners (NBPs) and NE components of the Linker of Nucleoskeleton and Cytoskeleton (LINC) complexes, to transfer on the nuclear matrix forces that are generated by the cytoskeleton and that travel through the nucleus's outer and inner membranes via LINC complexes [5–10]. Mutations in emerin that impact its interactions with NBPs and its self-assembly into nanodomains, such as Δ95-99, Q133H, or P183H mutations [1,5,11–13], correlate with abnormal responses of the NE to mechanical stress [5]. In cells exposed to extensive forces, such as skeletal and cardiac cells, these aberrant responses result in Emery-Dreifuss muscular dystrophy (EDMD) [14].

Numerous studies have highlighted the significance of emerin's disordered region for its biological function in nuclear mechanics [5,11–13]. This region mediates emerin self-assembly as well as binding to NBPs that regulate the

*Contact author: pinaud@usc.edu
†Contact author: cah77@usc.edu

nuclear architecture, including lamins, nuclear actin, LINC complex proteins, and other molecular partners [1,15]. The expected structural flexibility of its disordered region likely allows emerin to adopt various conformations that, in turn, modulate emerin's self-assembly and its engagement with different NBPs at the INM. Biochemistry studies have indeed indicated that wild-type (WT) emerin is associated with two different nucleoskeletal neighborhoods at the NE [16] and recent single-molecule imaging studies have revealed that at the steady state, it distributes into rapidly and slowly diffusing emerin populations, the latter forming stable INM nanodomains characterized by elevated emerin concentrations [5]. Those imaging studies also showed that adequate nuclear responses to mechanical challenges induced by cell micropatterning require controlled changes in the diffusion properties and spatial organization of both types of emerin complexes [5]. In effect, compared to WT emerin, the aforementioned EDMD-inducing emerin mutants display either insufficient or excessive self-assembly into nanodomains, both of which result in defective nuclear shape adaptations against force [5]. Modulation of the self-assembly of emerin into INM nanodomains is therefore a central determinant of NE response to forces as it prevents deleterious nucleus deformations typically observed in EDMD.

The spatial patterns of emerin observed at the INM, the distinction between slowly and rapidly diffusing emerin complexes, and the observed dependence of emerin nanodomains on emerin diffusion are reminiscent of molecular patterns resulting from reaction-diffusion processes [17–19]. In this Letter, we combine theory and experiment to explain the observed self-assembly of emerin nanodomains in terms of a reaction-diffusion (Turing) model of emerin complexes. After

validating our model for WT emerin under no mechanical stress, we employ our model to understand how and why WT emerin nanodomains respond to force application. We then use our model to connect defects in the nanoscale organization of EDMD-associated emerin mutants to changes in key reaction and diffusion properties of emerin and its NBPs. Our results suggest that the self-assembly and plasticity of emerin nanodomains result from the interaction of slowly diffusing emerin complexes that can locally bind other emerin, and rapidly diffusing emerin complexes that inhibit increased molecule concentrations through steric constraints.

Modeling emerin nanodomains. Super-resolution microscopy experiments on emerin nanodomains report the diffusion coefficients of rapidly and slowly diffusing emerin populations at the INM, the size of emerin nanodomains, and their molecular density along the INM [5]. The question thus arises to what extent the observed emerin densities along the INM can be accounted for based on the measured emerin diffusion coefficients together with the observed nanodomain sizes. We have addressed this question through a simple model of emerin diffusion in heterogeneous media (see Supplemental Material [20,21]). We find that this model yields, with no adjustable parameters, the observed localization of WT emerin to nanodomains, without the need to invoke cellular structures that confine emerin to particular membrane regions. These results suggest that the observed distributions of emerin along the INM can be understood quantitatively based on emerin's diffusion properties, which we take as our starting point for modeling the self-assembly of emerin nanodomains.

Slowly diffusing emerin is thought to interact with NBPs so as to facilitate binding to other emerin, while rapidly diffusing emerin also interacts with NBPs but is not thought to produce higher-order emerin structures [5]. In our model of emerin nanodomain self-assembly, we therefore allow for slowly and rapidly diffusing emerin-NBP complexes at the INM with distinct emerin and NBP binding properties. We denote these two types of emerin-NBP complexes by A and I with diffusion coefficients ν_A and $\nu_I > \nu_A$, respectively. We assume that the slowly diffusing A complexes can transiently bind other emerin or NBPs to locally increase the concentration of A and I. In contrast, we assume that the rapidly diffusing I complexes do not bind other emerin or NBPs, but can crowd the INM. Thus, A complexes locally *activate* increased concentrations of A and I, while I complexes *inhibit* increased concentrations of A and I through steric constraints. To see how these reaction-diffusion properties of emerin can yield nanodomain self-assembly via a Turing mechanism, consider a random distribution of I and A complexes along the INM [22]. If, at some INM location, there is a local excess of A over I, then A will tend to locally increase the concentrations of both A and I. Since I complexes diffuse away more rapidly, this produces a positive feedback elevating the concentration of emerin molecules at that INM location. Eventually, a steady state is reached when enough I complexes are drawn in to balance the local population of A complexes, producing a stable pattern of emerin nanodomains.

To quantify the above mechanism for emerin nanodomain self-assembly it is necessary to specify reactions between I and A complexes, for which we employ experiments on WT emerin [5]. While we show here that the emerin-NBP

interactions captured by I and A complexes at the INM are sufficient to produce the observed emerin nanodomains, we also note that the rapidly and slowly diffusing emerin populations seen in experiments most likely encompass more than just these two types of molecular complexes, which a more detailed model would take into account. Based on observations that before it accumulates at the INM, emerin distributes in the endoplasmic reticulum and outer nuclear membranes where no NBPs are present, we assume that I and A complexes in the INM can assemble from or dissociate into pools of emerin and NBPs that lack the molecular requirements to form I or A complexes, and denote the corresponding molecules by $\varnothing$. For simplicity, we take the spontaneous assembly of I and A complexes to be negligible compared to their spontaneous disassembly, $I \xrightarrow{f_1} \varnothing$ and $A \xrightarrow{g_1} \varnothing$ with disassociation rates f_1 and g_1. In the Supplemental Material [21] associated with this Letter, we consider a more general version of our model that also allows for the spontaneous assembly of I and A complexes.

When imaging WT emerin, rapidly diffusing emerin are primarily observed outside emerin nanodomains of diameter 22 ± 11 nm, while slowly diffusing emerin are primarily found inside nanodomains [5]. Taking the "typical" maximum size of WT emerin nanodomains to correspond to the mean size plus one standard deviation, we thus expect that I complexes are able to diffuse over a scale of about one-half of 33 nm. Since A complexes are nearly immobile at the INM [5], we assume that A complexes stay localized to molecular length scales, which we set at ~ 1 nm. From the root-mean-square displacements $2\sqrt{\nu_I/f_1}$ and $2\sqrt{\nu_A/g_1}$, we thus estimate $f_1 \approx 30$ s^{-1} and $g_1 \approx 40 f_1$ for the diffusion coefficients $\nu_I \approx 2 \times 10^{-3}$ μm^2/s and $\nu_A \approx 3 \times 10^{-4}$ μm^2/s measured for WT emerin [5]. These values of f_1 and g_1 can be changed by $>50\%$ in our model to obtain WT emerin nanodomains with similar properties.

As mentioned in the introduction, emerin has a large disordered domain with multiple binding sites, for both NBPs and other emerin. At the most basic level, single A complexes may thus produce local increases in the emerin concentration by facilitating the formation of I and A complexes, $A + \varnothing \xrightarrow{f_2} A + I$ and $A + \varnothing \xrightarrow{g_2} 2A$. Since A complexes are known to produce higher-order structures [5], we also allow for the simplest higher-order reaction $2A + \varnothing \xrightarrow{g_3} 3A$, in which two A complexes facilitate the formation of another A complex. We estimate the values of the reaction rates f_2, g_2, and g_3 from f_1 and g_1. In particular, experiments on WT emerin indicate that nanodomains are predominantly composed of A, rather than I, complexes [5], suggesting that $f_2 < f_1$. Here we set $f_2 = f_1/2$ for WT emerin. Due to the slow diffusion of A complexes, the leading-order dissociation and assembly rates of A complexes must be approximately equal to each other so that a nontrivial steady state can be achieved. We thus set $g_2 = g_1$ for WT emerin. Finally, we assume that as specified mathematically below, higher-order reactions have a smaller propensity to occur than lower-order reactions. We therefore set $g_3 = g_2/10$ for WT emerin. Other choices for the values of f_2, g_2, and g_3 give similar results for WT emerin provided that $f_2 \lesssim f_1$, $g_1 \approx g_2$, and $g_3 \ll g_2$.

We quantify the fractional area coverage of I and A complexes at a particular INM location (x, y) and time t by the

fields $I(x, y, t)$ and $A(x, y, t)$ with $0 \leqslant I \leqslant 1$ and $0 \leqslant A \leqslant 1$, where the upper bounds on I and A account for steric constraints. We rescale the rates of all reaction and diffusion processes locally increasing I or A by a steric factor $S = 1 - I - A$ so as to ensure that $0 \leqslant I + A \leqslant 1$. At the mean-field level, I and A are then governed by the reaction-diffusion equations [22–25],

$$\frac{\partial I}{\partial t} = F(I, A) + \nu_I \nabla \cdot [(1 - A)\nabla I + I \nabla A], \quad (1)$$

$$\frac{\partial A}{\partial t} = G(I, A) + \nu_A \nabla \cdot [(1 - I)\nabla A + A \nabla I], \quad (2)$$

where the polynomials F and G describe the aforementioned reaction dynamics of I and A complexes,

$$F(I, A) = -f_1 I + f_2 S A, \quad (3)$$

$$G(I, A) = -g_1 A + g_2 S A + \frac{g_3}{2\bar{A}} S A^2, \quad (4)$$

and we denote the values of I and A at the homogeneous steady state $F = G = 0$ by $\bar{I}$ and $\bar{A}$, respectively. The factor $1/2$ in the last term in Eq. (4) arises because this term describes a second-order reaction involving two (indistinguishable) A complexes [25]. Furthermore, we rescale g_3 in Eq. (4) by the characteristic value $A = \bar{A}$ so as to permit direct numerical comparisons of g_2 and g_3, which allows us to fix g_3 in terms of g_2 so that $g_3 \ll g_2$, even though these two parameters are associated with reactions of different order. Note that $\bar{I}$ and $\bar{A}$ depend on all reaction rates in the model (see Supplemental Material [21]). The biophysical reasoning above fixes the approximate values of all parameters in Eqs. (1) and (2) for WT emerin, which we then use to investigate the effect of applied forces and mutations on emerin nanodomains. Within the general mathematical constraints imposed by Turing patterns, other parameter values can give similar results (see Supplemental Material [21]). Our results are robust with respect to perturbations in the values of the reaction rates and diffusion coefficients considered here. To study the self-assembly of emerin nanodomains, we numerically solve Eqs. (1) and (2) starting from random initial conditions about $(I, A) = (\bar{I}, \bar{A})$ (see Supplemental Material [21]).

Organization of WT emerin. We validate our reaction-diffusion model of emerin nanodomain self-assembly based on experiments on WT emerin at the INM [5]. For the parameter values described above, Eqs. (1) and (2) yield, starting from random initial conditions, spontaneous self-assembly of emerin nanodomains [see Fig. 1(a)]. We quantify the size of these nanodomains through a linear stability analysis to calculate the characteristic nanodomain diameter ℓ implied by Eqs. (1) and (2) (see Supplemental Material [21]). We find $\ell \approx 20$ nm in the steady state of the system, which agrees with the nanodomain diameter measured for WT emerin, $\ell = 22 \pm 11$ nm [5], and the numerical solutions in Fig. 1(a). In agreement with experimental observations, we find that the emerin populations in WT nanodomains are dominated by the slowly diffusing A complexes rather than the rapidly diffusing I complexes [Fig. 1(a)]. We obtained results similar to those shown in Fig. 1(a) when we allowed for additional steric effects arising from a pool of emerin (or other NBPs) not
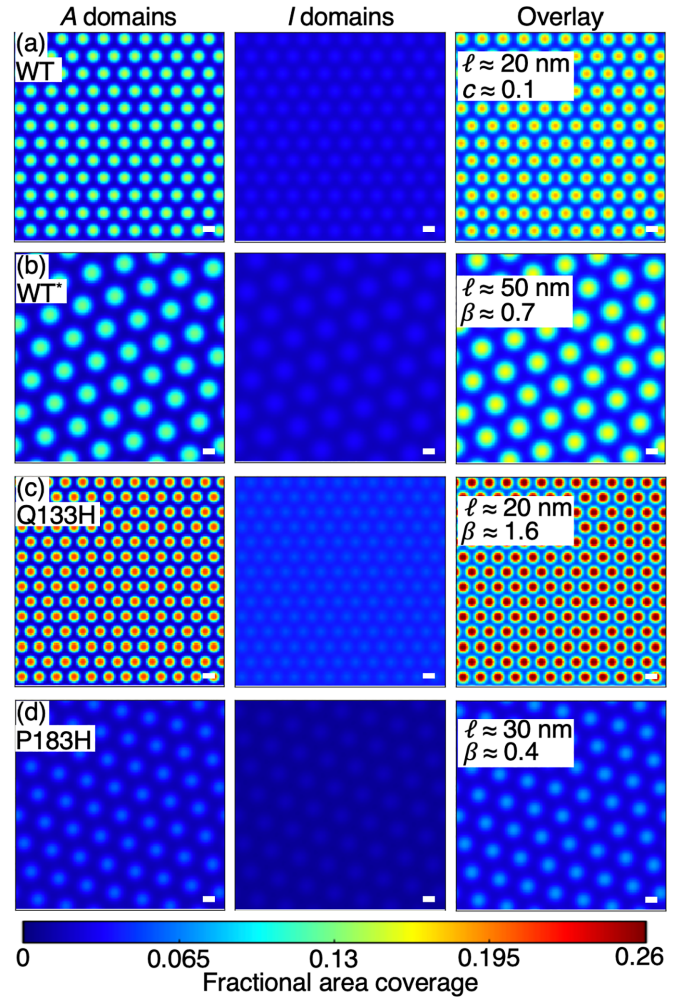

FIG. 1. Numerical solutions of Eqs. (1) and (2) with Eqs. (3) and (4) for (a) WT emerin, (b) WT emerin under force (WT*), (c) Q133H emerin, and (d) P183H emerin. All solutions correspond to steady states of Eqs. (1) and (2) with Eqs. (3) and (4) obtained from random initial conditions at $t = 0$. The left, middle, and right density maps show $A(x, y, t), I(x, y, t)$, and $A(x, y, t) + I(x, y, t)$ at $t = 100\tau$, respectively, where the characteristic timescale τ follows from a linear stability analysis and is given by (a) $\tau \approx 6$ s, (b) $\tau \approx 17$ s, (c) $\tau \approx 3$ s, and (d) $\tau \approx 32$ s (see Supplemental Material [21]). The values of the reaction and diffusion parameters in Eqs. (1) and (2) with Eqs. (3) and (4) were chosen as explained in the main text. Scale bars, 20 nm.

accounted for through I and A complexes (see Supplemental Material [21]).

We establish further links between our model results and experimental observations through the average fraction of the nanodomain area covered by I and A complexes, which we denote by c. To estimate c from numerical solutions of Eqs. (1) and (2), we first find, for a given nanodomain, the grid point associated with the maximum of $(I + A)$ in the steady state of the system. We then average $(I + A)$ over all grid points within a radius $\ell/2$, rounded to the nearest multiple of the grid spacing, about this (local) maximum of $(I + A)$. We carry out this procedure for five nanodomains and average the results to obtain c. This last step was, strictly speaking, not necessary

since c evaluated over a single nanodomain and c evaluated over multiple nanodomains yield similar results. We estimate c from experiments based on the measured emerin numbers in nanodomains, the measured diameter of nanodomains, and the INM area occupied by emerin ($\approx$1–4 nm^2) (see Supplemental Material [21]). We find $c \approx 0.1$ from Eqs. (1) and (2), with experiments on WT emerin giving the values $c \approx 0.03$–0.1 [21].

The above results show that Eqs. (1) and (2) yield a WT emerin nanodomain diameter ℓ and fractional area coverage c close to experimental estimates. However, a few notable discrepancies between experiment and theory deserve comment. First, we note that our model produces closely spaced nanodomains with a uniform size and shape, while experiments show nanodomains with irregular sizes and shapes that tend to be more widely spaced than the nanodomains in Fig. 1(a) (see Supplemental Material [5,21]). This discrepancy arises, on the one hand, from the mean-field character of Eqs. (1) and (2), which neglect molecular noise. Such noise can produce irregular domain shapes, sizes, and spacings, and even result in domain linkage (see Supplemental Material [21,26]). On the other hand, we note that the INM contains large membrane structures, such as nuclear pore complexes, that restrict the membrane area available for emerin nanodomain self-assembly, and thus increase the effective separation of emerin nanodomains seen in experiments (see Supplemental Material [21]). Furthermore, the value of c predicted from Eqs. (1) and (2) is at the upper bound of the range of values of c suggested by experiments. This discrepancy likely arises because, due to a lack of detailed experimental data on how emerin interacts with NBPs in nanodomains, we only consider the size of emerin when estimating c from experiments and thus effectively neglect the finite size of NBPs (see Supplemental Material [21]). As a result, our experimental estimates of c likely underestimate c. Similar considerations apply to the scenarios we consider next.

Organization of WT emerin under force (WT⋆). Constraining cells within micropatterns narrower than their typical size offers a simple means to impose steady-state mechanical stress on the nucleus (see Supplemental Material [21,27]). Subjecting cells to nuclear mechanical stress using 10- or 15-μm-wide micropatterns induces an increase in WT emerin nanodomain size by approximately threefold, from $\ell = 22 \pm 11$ to $\ell = 60 \pm 13$ nm [5]. Furthermore, the value of c observed experimentally for WT⋆ emerin nanodomains is a fraction $\beta \approx 0.6$ of the value of c found for WT nanodomains. Experiments further indicate that possibly due to a mechanical stress-induced disruption in the interactions between emerin and NBPs, the diffusion coefficients ν_I and ν_A are approximately doubled for WT⋆ emerin as compared to WT emerin, with $\nu_I = 4 \times 10^{-3}$ μm^2/s and $\nu_A = 6 \times 10^{-4}$ μm^2/s [5].

Adjusting ν_I and ν_A in our model to account for WT⋆ emerin while using the same reaction dynamics as for WT emerin, we found that ℓ increased to $\ell \approx 30$ nm with $\beta \approx 0.9$. This suggests that the observed changes in ν_I and ν_A can partially, but not fully, account for the observed changes in the size and density of WT emerin nanodomains under force. Considering the reduced experimental value of β for WT⋆ nanodomains, we hypothesized that a major effect of mechanical stress on the emerin reaction properties is to weaken

emerin's ability to form higher-order complexes, which could arise from stress-induced changes in the organization and binding of NBPs. Some support for this picture is provided by experiments in which the binding of nuclear actin to WT emerin was reduced by depletion of nuclear actin in cells, which yielded less dense but bigger emerin nanodomains, mimicking the changes in WT emerin nanodomains observed under mechanical stress [5]. To test whether such a modification of the reaction dynamics can explain the observed changes in nanodomain size and density, we decreased g_3 by 50%, to $g_3 = g_2/20$ [see Fig. 1(b)]. This modification increased the nanodomain size to $\ell \approx 50$ nm with $\beta \approx 0.7$. Decreasing g_3 further by 10% relative to g_2 resulted in $\ell \approx 60$ nm and $\beta \approx 0.6$. Thus, the observed increases in the emerin diffusion coefficients together with a decrease in the relative strength of higher-order interactions seem to underlie the observed response of WT emerin nanodomains to mechanical stress.

Organization of Q133H emerin mutant. The Q133H mutation of emerin was observed to yield nanodomains of diameter $\ell = 19 \pm 12$ nm under no mechanical stress, which is statistically identical to the nanodomain size $\ell \approx 20$ nm associated with WT emerin, while the emerin density in Q133H nanodomains was increased by approximately 50% compared to WT emerin, $\beta \approx 1.5$ [5]. Furthermore, Q133H emerin was found to diffuse somewhat more rapidly than WT emerin, with the diffusion coefficients $\nu_I \approx 3 \times 10^{-3}$ μm^2/s and $\nu_A \approx 4 \times 10^{-4}$ μm^2/s [5]. Adjusting ν_I and ν_A in our model to account for Q133H emerin but using the same reaction dynamics as for WT emerin, we found that ℓ increased by 10% while c remained approximately unchanged compared to WT emerin. Thus, the observed changes in Q133H emerin nanodomains seem to rely on changes in the emerin reaction properties.

It has been proposed that the Q133H mutation of emerin increases the potential of emerin-NBP complexes to bind additional emerin [5]. We can quantify and test this hypothesis by noting that in our model, A complexes represent emerin-NBP complexes that can bind additional emerin. We therefore assume that the Q133H mutation of emerin leads to a more pronounced dependence of the reaction dynamics in Eqs. (3) and (4) on reactions driven by A complexes, which we implemented through a uniform percentage increase in the strength of these reactions. Figure 1(c) shows model results obtained with an increase by 30% in f_2, g_1, g_2, and g_3 compared to WT emerin. In agreement with experiments, we now find Q133H emerin nanodomains with a diameter $\ell \approx 20$ nm and $\beta \approx 1.6$. The agreement between model results and experiments suggests that the observed changes in Q133H nanodomains result from more rapid emerin diffusion together with an elevated propensity of emerin-NBP complexes to bind additional emerin.

Organization of P183H emerin mutant. The P183H mutation of emerin was observed to yield nanodomains with a diameter $\ell = 35 \pm 12$ nm and an emerin density in nanodomains that was decreased by approximately 70% compared to WT emerin, $\beta \approx 0.3$ [5]. Furthermore, P183H emerin was observed to diffuse more slowly than WT emerin, with the diffusion coefficients $\nu_I \approx 1 \times 10^{-3}$ μm^2/s and $\nu_A \approx 1 \times 10^{-4}$ μm^2/s [5]. Adjusting ν_I and ν_A in our WT model to account for P183H emerin but not changing any reaction rates,
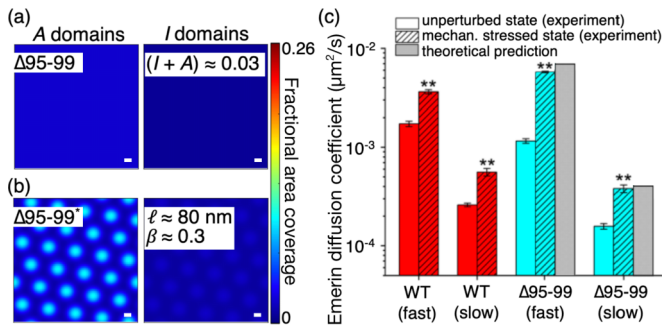
FIG. 2. Numerical solutions of Eqs. (1) and (2) with Eqs. (3) and (4) at $t = 100\tau$ as in Fig. 1, but for (a) $\Delta95$-99 emerin with $\tau \approx 128$ s and (b) $\Delta95$-$99^{\star}$ emerin with $\tau \approx 65$ s. Scale bars, 20 nm. (c) Measured and predicted diffusion coefficients of $\Delta95$-$99^{\star}$ emerin. The corresponding diffusion coefficients of WT and $\Delta95$-99 emerin are shown for comparison. T-test for experimental results on unperturbed vs mechanically stressed cells (**): $p < 0.01$.

we find $\ell \approx 10$ nm and $\beta \approx 1.1$. Thus, similarly as for Q133H emerin, the observed changes in P183H emerin nanodomains seem to rely on changes in the emerin reaction properties.

The P183H mutation of emerin is thought to decrease the potential of emerin-NBP complexes to bind additional emerin [5]. Decreasing, in analogy to Q133H, f_2, g_1, g_2, and g_3 by 30% compared to WT emerin, we find emerin nanodomains that were smaller and more dense than the nanodomains observed in experiments on P183H emerin, with $\ell \approx 20$ nm and $\beta \approx 0.7$. We reasoned that similar to the case of WT* emerin, the P183H mutation may produce a decrease in the relative strength of higher-order interactions facilitating the assembly of emerin complexes. Figure 1(d) shows model results obtained for P183H emerin with, in analogy to Q133H and WT* emerin, a decrease in f_2, g_1, and g_2 by 30%, but a decrease in g_3 by 60% compared to WT emerin. In agreement with experiments, we find P183H nanodomains with a diameter $\ell \approx 30$ nm and $\beta \approx 0.4$. Thus, the observed changes in P183H nanodomains appear to rely on a decreased propensity of emerin-NBP complexes to bind additional emerin, together with a decrease in the relative strength of higher-order interactions that facilitate the assembly of emerin complexes.

Organization of $\Delta95$-99 emerin mutant. In the absence of mechanical stress, the $\Delta95$-99 mutation of emerin was observed to yield an approximately random emerin distribution across the INM, with little-to-no nanodomain formation, and with diffusion coefficients $\nu_I \approx 1 \times 10^{-3}$ $\mu m^2/s$ and $\nu_A \approx 2 \times 10^{-4}$ $\mu m^2/s$ for the rapidly and slowly diffusing emerin populations [5]. We hypothesized that similarly as for P183H emerin, the $\Delta95$-99 mutation of emerin decreases the potential of emerin-NBP complexes to bind additional emerin. Taking, for simplicity, the reaction dynamics of $\Delta95$-99 emerin to be identical to those of P183H emerin in Fig. 1(d), we find that Eqs. (1) and (2) yield, for the diffusion coefficients measured for $\Delta95$-99 emerin, homogeneous I and A distributions and no nanodomains [see Fig. 2(a)]. Similar results are obtained when the strength of the reactions in Eqs. (3) and (4) driven by A complexes is decreased uniformly by as little as 20% compared to WT emerin. Thus, we find that a decreased propensity of emerin-NBP complexes to bind

additional emerin with, compared to P183H emerin, more rapid diffusion of A complexes seems to underlie the failure of $\Delta95$-99 emerin to self-assemble into nanodomains.

Organization of $\Delta95$-99 emerin under force ($\Delta95$-$99^{\star}$). Although diffusion coefficients for $\Delta95$-$99^{\star}$ emerin were not measured in previous experiments [5], it was observed that mechanical stress, induced by placing cells into 10 μm micropatterns, yields $\Delta95$-$99^{\star}$ nanodomains with an increased diameter, $\ell = 75 \pm 20$ nm, and a decreased emerin density, $\beta \approx 0.3$, compared to WT (and WT*) emerin [5]. We combined these experimental observations with our model results to estimate the reaction and diffusion properties of $\Delta95$-$99^{\star}$ emerin. In particular, based on our results for WT* emerin, we expect mechanical stress to weaken interactions between emerin and NBPs so as to decrease g_3 and increase ν_A. In analogy to WT* emerin, we therefore reduced g_3 by 50% compared to $\Delta95$-99 emerin in Fig. 2(a) and increased ν_A by a factor of two, to $\nu_A \approx 4 \times 10^{-4}$ $\mu m^2/s$. We hypothesized that the combined effects of the $\Delta95$-99 mutation and of mechanical stress largely decouple I from NBPs, such that $\Delta95$-$99^{\star}$ emerin shows a more pronounced increase in ν_I than in ν_A. Upon increasing ν_I from the value $\nu_I \approx 1 \times 10^{-3}$ $\mu m^2/s$ measured for $\Delta95$-99 emerin in the absence of mechanical stress, we find that a sevenfold increase in ν_I, to $\nu_I \approx 7 \times 10^{-3}$ $\mu m^2/s$, yields self-assembly of $\Delta95$-$99^{\star}$ nanodomains that are similar to those found experimentally, with $\ell \approx 80$ nm and $\beta \approx 0.3$ [see Fig. 2(b)].

To test the robustness of our model and assess whether our theoretical predictions of ν_A and ν_I for $\Delta95$-$99^{\star}$ emerin align with experiments, we proceeded to experimentally measure the diffusion coefficients of $\Delta95$-$99^{\star}$ emerin at the INM for cells that were mechanically stressed on 10 μm micropatterns, as in Ref. [5]. We found slowly and rapidly diffusing $\Delta95$-$99^{\star}$ emerin populations with $\nu_A = (3.8 \pm 0.3) \times 10^{-4}$ $\mu m^2/s$ and $\nu_I = (5.8 \pm 0.1) \times 10^{-3}$ $\mu m^2/s$, respectively, similar to our theoretical predictions [see Fig. 2(c)]. Interestingly, Eqs. (1) and (2) do not yield emerin nanodomains for these specific values of ν_A and ν_I if, as for WT* emerin, g_3 is reduced by 50% compared to $\Delta95$-99 emerin in Fig. 2(a), but Eqs. (1) and (2) do yield $\Delta95$-$99^{\star}$ nanodomains if g_3 is reduced by (slightly) less than 50%. For instance, decreasing g_3 by 45% compared to $\Delta95$-99 emerin in Fig. 2(a) while setting $\nu_A = 3.8 \times 10^{-4}$ $\mu m^2/s$ and $\nu_I = 5.8 \times 10^{-3}$ $\mu m^2/s$, Eqs. (1) and (2) yield emerin nanodomains that are similar to those in Fig. 2(b) and found experimentally for $\Delta95$-$99^{\star}$ emerin, with $\ell \approx 80$ nm and $\beta \approx 0.3$. Thus, the combined effects of more rapid diffusion of I and A complexes, with a greater percentage increase in ν_I than in ν_A, and a decrease in the relative strength of higher-order interactions seem to underlie the force-induced transition from a random distribution of $\Delta95$-99 emerin to self-assembled emerin nanodomains observed in experiments [5].

Conclusion. We have introduced here a simple physical model that describes quantitatively the self-assembly of emerin nanodomains at the INM. Our model suggests that the self-assembly of emerin nanodomains can be understood from a Turing mechanism in which emerin forms slowly or rapidly diffusing complexes with NBPs that activate or inhibit local increases in emerin concentrations at the INM, respectively. The model predicts that rapidly diffusing emerin play a critical

role in the self-assembly of stable emerin nanodomains, as initially implied by super-resolution imaging experiments that allowed a quantitative characterization of slowly and rapidly diffusing emerin populations at the INM. On the one hand, we showed how the measured diffusion properties of emerin can give rise to the observed supramolecular organization of emerin. On the other hand, our model establishes a connection between observed changes in the supramolecular organization and associated biological roles of emerin and modifications in key molecular properties of emerin. In particular, our model suggests key changes in the reaction and diffusion properties

of emerin underlying the observed alterations of emerin nanodomains under mechanical stress and EDMD-associated mutations of emerin. The model described here thus provides physics-based avenues for the control of emerin nanodomain self-assembly through modification of emerin reaction or diffusion properties.

[1] J. M. Berk, K. E. Tifft, and K. L. Wilson, The nuclear envelope lem-domain protein emerin, Nucleus **4**, 298 (2013).

[2] A. J. Koch and J. M. Holaska, Emerin in health and disease, Semin. Cell Dev. Biol. **29**, 95 (2014).

[3] J. Lammerding, J. Hsiao, P. C. Schulze, S. Kozlov, C. L. Stewart, and R. T. Lee, Abnormal nuclear shape and impaired mechanotransduction in emerin-deficient cells, J. Cell Biol. **170**, 781 (2005).

[4] A. C. Rowat, J. Lammerding, and J. H. Ipsen, Mechanical properties of the cell nucleus and the effect of emerin deficiency, Biophys. J. **91**, 4649 (2006).

[5] A. Fernandez, M. Bautista, L. Wu, and F. Pinaud, Emerin self-assembly and nucleoskeletal coupling regulate nuclear envelope mechanics against stress, J. Cell Sci. **135**, jcs258969 (2022).

[6] A. Méjat and T. Misteli, Linc complexes in health and disease, Nucleus **1**, 40 (2010).

[7] D. I. Kim, K. C. Birendra, and K. J. Roux, Making the LINC: Sun and kash protein interactions, Biol. Chem. **396**, 295 (2015).

[8] M. Crisp, Q. Liu, K. Roux, J. Rattner, C. Shanahan, B. Burke, P. D. Stahl, and D. Hodzic, Coupling of the nucleus and cytoplasm: Role of the LINC complex, J. Cell Biol. **172**, 41 (2006).

[9] M. L. Lombardi, D. E. Jaalouk, C. M. Shanahan, B. Burke, K. J. Roux, and J. Lammerding, The interaction between nesprins and sun proteins at the nuclear envelope is critical for force transmission between the nucleus and cytoskeleton, J. Biol. Chem. **286**, 26743 (2011).

[10] W. Chang, H. J. Worman, and G. G. Gundersen, Accessorizing and anchoring the LINC complex for multifunctionality, J. Cell Biol. **208**, 11 (2015).

[11] J. M. Berk, D. N. Simon, C. R. Jenkins-Houk, J. W. Westerbeck, L. M. Grønning-Wang, C. R. Carlson, and K. L. Wilson, The molecular basis of emerin–emerin and emerin–BAF interactions, J. Cell Sci. **127**, 3956 (2014).

[12] I. Herrada, C. Samson, C. Velours, L. Renault, C. Östlund, P. Chervy, D. Puchkov, H. J. Worman, B. Buendia, and S. Zinn-Justin, Muscular dystrophy mutations impair the nuclear envelope emerin self-assembly properties, ACS Chem. Biol. **10**, 2733 (2015).

[13] C. Samson, F. Celli, K. Hendriks, M. Zinke, N. Essawy, I. Herrada, A.-A. Arteni, F.-X. Theillet, B. Alpha-Bazin, J. Armengaud, C. Coirault, A. Lange, and S. Zinn-Justin, Emerin self-assembly mechanism: Role of the Lem domain, FEBS J. **284**, 338 (2017).

[14] A. E. Emery and F. E. Dreifuss, Unusual type of benign x-linked muscular dystrophy, JNNP **29**, 338 (1966).

[15] F. Haque, D. Mazzeo, J. T. Patel, D. T. Smallwood, J. A. Ellis, C. M. Shanahan, and S. Shackleton, Mammalian sun protein interaction networks at the inner nuclear membrane and their role in laminopathy disease processes, J. Biol. Chem. **285**, 3487 (2010).

[16] J. M. Berk, S. Maitra, A. W. Dawdy, J. Shabanowitz, D. F. Hunt, and K. L. Wilson, O-linked β-N-acetylglucosamine (O-GlcNAc) regulates emerin binding to barrier to auto-integration factor (BAF) in a chromatin- and lamin B-enriched Niche, J. Biol. Chem. **288**, 30192 (2013).

[17] A. M. Turing, The chemical basis of morphogenesis, Philos. Trans. R. Soc. London B **237**, 37 (1952).

[18] I. R. Epstein and J. A. Pojman, *An Introduction to Nonlinear Chemical Dynamics* (Oxford University Press, New York, 1998).

[19] A. Bailles, E. W. Gehrels, and T. Lecuit, Mechanochemical principles of spatial and temporal patterns in cells and tissues, Annu. Rev. Cell Dev. Biol. **38**, 321 (2022).

[20] Y. Li, O. Kahraman, and C. A. Haselwandter, Distribution of randomly diffusing particles in inhomogeneous media, Phys. Rev. E **96**, 032139 (2017).

[21] See Supplemental Material at http://link.aps.org/supplemental/10.1103/PhysRevResearch.7.L012019, which includes Refs. [28–34], for (i) details on the measurement of the diffusion coefficients and cluster maps for Δ95-99* emerin, (ii) estimates of the emerin concentration at the NE, (iii) analysis of emerin diffusion in heterogeneous media, (iv) a linear stability analysis of Eqs. (1)–(4) and details on the numerical solution procedure used here, (v) evaluation of spontaneous self-assembly of I and A complexes, (vi) assessment of crowding effects due to background pools of emerin or NBPs, and (vii) characterization of heterogeneity in emerin nanodomain size, shape, and arrangement.

[22] C. A. Haselwandter, M. Kardar, A. Triller, and R. A. da Silveira, Self-assembly and plasticity of synaptic domains through a reaction-diffusion mechanism, Phys. Rev. E **92**, 032705 (2015).

[23] J. E. Satulovsky, Lattice Lotka-Volterra models and negative cross-diffusion, J. Theor. Biol. **183**, 381 (1996).

[24] C. A. Lugo and A. J. McKane, Quasicycles in a spatial predator-prey model, Phys. Rev. E **78**, 051911 (2008).

[25] Y. Li, O. Kahraman, and C. A. Haselwandter, Stochastic lattice model of synaptic membrane protein domains, Phys. Rev. E **95**, 052406 (2017).

[26] E. Law, Y. Li, O. Kahraman, and C. A. Haselwandter, Stochastic self-assembly of reaction-diffusion patterns

in synaptic membranes, Phys. Rev. E **104**, 014403 (2021).

[27] M. Bautista, A. Fernandez, and F. Pinaud, A micropatterning strategy to study nuclear mechanotransduction in cells, Micromachines **10**, 810 (2019).

[28] A. Getis and J. Franklin, Second-order neighborhood analysis of mapped point patterns, Ecology **68**, 473 (1987).

[29] S. Eskandari, E. M. Wright, M. Kreman, D. M. Starace, and G. A. Zampighi, Structural analysis of cloned plasma membrane proteins by freeze-fracture electron microscopy, Proc. Natl. Acad. Sci. USA **95**, 11235 (1998).

[30] C. A. Haselwandter, M. Calamai, M. Kardar, A. Triller, and R. A. da Silveira, Formation and stability of

synaptic receptor domains, Phys. Rev. Lett. **106**, 238104 (2011).

[31] O. Kahraman, Y. Li, and C. A. Haselwandter, Stochastic single-molecule dynamics of synaptic membrane protein domains, EPL **115**, 68006 (2016).

[32] J. Bezanson, A. Edelman, S. Karpinski, and V. B. Shah, Julia: A fresh approach to numerical computing, SIAM Rev. **59**, 65 (2017).

[33] C. Rackauckas and Q. Nie, DifferentialEquations.jl—a performant and feature-rich ecosystem for solving differential equations in Julia, J. Open Res. Softw. **5**, 15 (2017).

[34] D. H. Lin and A. Hoelz, The structure of the nuclear pore complex (an update), Annu. Rev. Biochem. **88**, 725 (2019).